MultiRS Flood Mapper: A Google Earth Engine Application for Water Extent Mapping with Multimodal Remote Sensing and Quantile-Based Postprocessing

Zhouyayan Li [a,b*], Ibrahim Demir [a,b,c]

[a] Dept. of Civil and Environmental Engineering, University of Iowa, Iowa City, Iowa, USA
[b] IIHR Hydroscience and Engineering, University of Iowa, Iowa City, Iowa, USA
[c] Dept. of Electrical and Computer Engineering, University of Iowa, Iowa City, Iowa, USA
* Corresponding Author, Email: zhouyayan-li@uiowa.edu

Abstract

Remote Sensing (RS) imagery is an important data source in surface water mapping applications thanks to its high spatial and temporal consistency and scalability. The introduction of Google Earth Engine (GEE) has cleared some of the major barriers of fast and large-scale RS-based geospatial analyses by providing easy and open access to most of the commonly used RS image products as well as built-in functions designed for geospatial analysis. There is a growing interest in developing GEE applications that can work for different regions and time durations to improve the reusability of GEE scripts and reduce manual effort during the entire workflow of water-body extraction. Despite all those advancements and efforts, there is still a need for creating GEE applications that are user-friendly and can serve both remote sensing experts and students. These applications are also expected to be powerful and comprehensive enough to handle each step along the entire lifecycle of water body extraction workflow and are capable of handling geomorphic and geospatial discrepancies between regions under various configurations. Given these needs and challenges, this study presents the MultiRS Flood Mapper, a GEE application that incorporates three most used RS imagery (i.e., Sentinel-1 SAR, Landsat 8, and Sentinel-2) in water body mapping and integrates advanced dynamic thresholding algorithms and powerful postprocessing modules to improve classification results under the influence of dense vegetation and cloud, and in regions with constrained hydraulic conditions. In addition, the MultiRS Flood Mapper comes with a self-explanatory and user-friendly interface. Most functional modules for RS image processing that require professional knowledge are fully automated and the remaining function in an intuitive and interactive way, which therefore enables the MultiRS Flood Mapper to have great potential to serve a broad audience with various backgrounds and purposes.

Keywords: image fusion; Google Earth Engine; multimodal remote sensing; flood mapping; cloud application

1. Introduction

Remote Sensing (RS) imagery is an essential data source for Earth surface observation with an increasing popularity over recent years. Compared to many traditional data-collecting approaches, such as instrumentation and field measurements (Muste et al., 2017) in the hydrology research domain, RS is more scalable and efficient in large regions (Kim et al., 2021). Compared to some of the newly emerged data-collection approaches, such as crowd-sourced data, RS has the advantage of being more spatially and temporarily consistent (Ali and Ogie, 2017; Li, Xiang, et al., 2022). One additional advantage of RS data is the global data availability. Many other data sources are not open to the public due to confidentiality and cost reasons or are just open to usage under limited conditions (Cretaux et al., 2023; Estoque, 2020).

In contrast, there are many RS image sources that are openly accessible, have global coverage, and come with appropriate spatial and temporal resolutions that can provide sufficient information for common Earth's surface modeling and analyses, such as wetland monitoring (Abdelmajeed et al., 2023), landslide mapping wildfire and flood forecasting (Xiang et al., 2021) and mapping (Ghali & Akhloufi, 2023; Sadiq et al., 2022), vegetation and crop monitoring (Cheng et al., 2020; Tsyganskaya et al., 2018), oil and gas (Torres Gil et al., 2023) mapping, and so on. In addition, RS imagery has become an indispensable data source for the emerging machine-learning-and-deep-learning-aided environmental analyses and applications (Demiray et al., 2021; Sit et al., 2021, 2023; Bayar et al., 2009).

Despite all those advantages and the potential, in the surface water mapping domain, there are still three main reasons preventing RS imagery from being used in more applications or being appreciated by a broader audience. The first reason is the domain knowledge needs. Unlike common daily-life imagery, an in-depth understanding of the mechanism during the whole-lifecycle of RS image generation is required to manipulate and derive useful information from those imagery. The second barrier, building on top of the first issue, is the verbose pre- and post-processing steps as well as the unavoidable manual adjustments during the analysis processes. The final blocker is high-end computational resources needs. RS images for Earth's surface observations often contain multiple bands and can be highly demanding for computational capacity and storage of the computers.

The introduction of Google Earth Engine (GEE) has greatly relieved many of those issues. Google Earth Engine is a cloud platform that is aimed at supporting geospatial analyses at the planetary scale (Gorelick et al., 2017). It has a comprehensive data repository that includes most of the commonly used datasets for Earth surface observation, and climate analysis and monitoring (Gorelick et al., 2017; Li & Demir, 2023b). With GEE, users no longer need to switch between different platforms where data is originally collected and distributed. Moreover, many image items on GEE have gone through substantial pre-processing and are very close to a ready-to-use level (Aravind et al., 2023). For instance, GEE conducted orbit metadata update, Analysis Ready Data (ARD) border noise removal, thermal noise removal, radiometric calibration, and terrain correction for every Sentinel-1 SAR image before serving it on the platform (Moothedan et al., 2020).

The preprocessing done by GEE is an important time and effort saver for users, because otherwise, users will need to utilize professional RS image processing software to go over each of those steps and process all images in a collection. The built-in objects and methods in GEE that are specifically designed for geospatial analyses and computations also make it way easier and faster for data manipulation and analysis (SAJAN et al., 2023; Waleed et al., 2023). Finally, as GEE is a cloud platform and all computations will be on GEE server, the requirement for computational resources on users' side is greatly reduced (Velastegui-Montoya et al., 2023). Thanks to GEE, global-level studies as well as studies that span a long period of time with fewer manual efforts are made possible (Amani et al., 2020; Tamiminia et al., 2020).

The interest in creating GEE applications to improve the reusability of GEE code and scripts and reducing the manual effort in the "revise code-run script-evaluate result-revise code" cycle has been increasing in recent years. Numbers of studies is on the rise that focused not on creating GEE scripts for a specific event but on implementing a GEE application that are reusable and can work with various configurations. For instance, Tripathy & Malladi, (2022) introduced Global Flood Mapper, a GEE application that applies z-score thresholding to SAR image series before and after the flooding to detect changes on the ground.

The Global Flood Mapper allows users to generate and download flood maps in regions following the administrative division of each country. Liu et al., (2018) proposed a Flood Prevention and Emergency Response System powered by GEE to support flood prevention and warning for Taiwan. Buettig et al. (2022) proposed WaterMaskAnalyzer (WMA), a GEE application that generates water extent maps by applying Otsu-thresholding methods to SAR, Sentinel-2, or Landsat 8 image following users' selection to custom study area and time window. Along with the main functionality of water mask generation, WMA supports four speckle filtering approaches for SAR image preprocessing.

Despite all those efforts and exciting advancements, there is still room for improvement. Specifically, some issues with many existing GEE applications in the surface water mapping domain include being a) static: Some applications are more of a demonstrator rather than a dynamic computational tool and can just showcase a fixed number of results based on users' selection; b) limited: Some applications come directly from previous projects that focus on specific regions and time durations, and the functionality of the application are still limited to those previous configurations; and c) simple: Many existing applications failed to consider the geomorphic and geospatial differences between regions and applied the same waterbody extraction method to all regions without sufficient postprocessing to handle the errors that could arise due to those differences. For some applications, not every necessary step of the RS-based water-body extraction workflow is implemented, and those applications are therefore more simplified versions with reduced utility.

To close those gaps, this study proposed a Google Earth Engine application for surface water extent mapping. The application, which will be referred to as MultiRS Flood Mapper hereafter, is compatible with the three most used RS image sources in water extent mapping applications, namely, Sentinel-1 SAR, Sentinel-2, and Landsat 8 images. The MultiRS Flood Mapper adopts

advanced dynamic water-body mapping approaches and integrates extra postprocessing modules to handle different geospatial and hydraulic conditions more effectively. The MultiRS Flood Mapper automates most functional modules for RS image processing (e.g., denoising SAR image, cloud removal for optical images, and dynamic thresholding for water body extractions) that require professional knowledge. Remaining modules for which manual adjustments are necessary are designed and implemented in an intuitive and user-friendly way.

The contribution of this work includes a) introducing an openly accessible water extent mapper to facilitate fast mapping, analyzing, and comparing the Earth's surface water body using multimodal RS images; b) incorporating advanced functional modules to improve the accuracy of classifications in several complex conditions (i.e., areas under the influence of cloud & cloud shadow and dense vegetation and areas with constrained hydraulic conditions); and c) designing and building the system with open data that has global coverage as well as with a user-friendly interface. In short, the MultiRS Flood Mapper is aimed at providing accurate and reliable water extent predictions derived from multimodal RS images to support fast flood-related risk analysis (Yildirim & Demir, 2022; Cikmaz et al., 2023), damage estimation (Alabbad et al., 2023) and decision-making (Yildirim et al., 2022; Alabbad and Demir, 2022) tasks for users with different backgrounds.

2. Data and Methodology

2.1. Data Integration

Data used by the MultiRS Flood Mapper falls into three categories: a) RS imagery, including two multispectral sources: Sentinel-2 and Landsat 8 surface reflectance, and one radar source: Sentinel-1 C-band SAR. To keep it simple, those three types of RS images will be referred to as SAR, S2, and L8, respectively; b) data to be used in postprocessing, including the DEM and Height Above the Nearest Drainage (HAND) layers; and c) auxiliary and optional data, including shapefiles that indicate the scope any hydraulic structures controlled. Table 1 lists more details about the abovementioned data items.

It is worth noting that the revisit cycle listed in Table 1 is the worst scenario. In regions that can be scanned by both satellites in the system, the revisit cycle will improve. For example, when considering both satellites in the Sentinel-1 system, the revisit cycle for some regions on the Earth will be improved to 6 days, and even shorter if overlaps from neighboring scans are also considered. We used two DEM products because the USGS 3DEP 10 m DEM is available only for the United States. HAND is a normalized elevation that measures how vertically far away any hillslope pixels are from the main water plane (e.g., river channel and lake water bodies) (Nobre et al., 2011; Rennó et al., 2008; Li and Demir, 2022).

It is a common postprocessing index to eliminate false-positive errors (pixels classified as water bodies but are actually dry) for water surface mapping using RS imagery (Chow et al., 2016; Pelich et al., 2017; Zhao et al., 2021). HAND is also a stand-along simplified flood model with its efficacy proven in many previous studies (Godbout et al., 2019; Komolafe et al., 2020;

Li et al., 2022, 2023; Li and Demir, 2024). Slope is derived from DEM on-the-fly when the postprocessing function is activated and thus not listed in Table 1 as a separate item.

Table 1. Details about the data used by the MultiRS Flood Mapper

Category	**Item**	**Spatial Resolution**	**Satellite Revisit Cycle**	**Data Source**	**Band Involved**
Remote Sensing Imagery	Sentinel-1 C-band SAR GRD	10 m	12 days	ESA[G]	VV
	Sentinel-2 Surface Reflectance	10 m for R, G, and B bands; 20 m for SWIR1	10 days	ESA[G]	Blue, Green, Red, SWIR1
	Landsat 8 OLI/TIRS Surface Reflectance	30 m	16 days	USGS[G]	Blue, Green, Red, SWIR1
Data for Post-processing	USGS 3DEP 10m DEM	10 m	-	USGS[G]	elevation
	NASA SRTM Digital Elevation	30 m	-	NASA[G]	elevation
	Global 90m Height Above the Nearest Drainage Map	90 m	-	(Gao et al., 2016)	b1
Optional	Scope controlled by hydraulic structures	-	-	User Input	-

G: Data that are openly available on Google Earth Engine

2.2. GEE Application Interface

As discussed in the Introduction section, the MultiRS Flood Mapper runs entirely on the cloud and anyone who has access to the internet can use it. Thanks to GEE, MultiRS Flood Mapper can easily access and process most items listed in Table 1 without relying on additional platforms or software. Using the built-in data structure and widgets, we were able to implement the app with a user-friendly GUI that supports complex user interaction and can facilitate the communication between the user and the backend to call built-in image processing functions available on the platform and return results.

Figure 1 shows the app interface when it is loaded for the first time. There is a non-functional introduction section right above the “Define Area of Interest” on the interface. That contains the name, a brief overview of the application, and some contact information of the authors. It is not displayed in Figure 1 because we want to make room for functional sections to facilitate discussions about them in this paper. We encourage readers to try the app for a better understanding of how every function is arranged on the webpage. To get the data ready, users will simply go over each item shown in Figure 1 from top to bottom and have them all set or selected.

Once the data is ready, users need to click the Get Flood Extent button at the bottom of the panel on the left in Figure 1 to generate a water extent. The extent map will be added to the left display zone upon creation and the interface will change upon the creation of the first map. Figure 2 shows the new interface after getting the first map. As can be seen by the user, we have

a new panel—the right one, and some additional items added to the bottom of the left panel. The newly added items on the left panel are functional components of a stronger postprocessing section, called the Quantile-based Filling & Refining (QFR). We will give a detailed description of the QFR section in subsection 2.3.

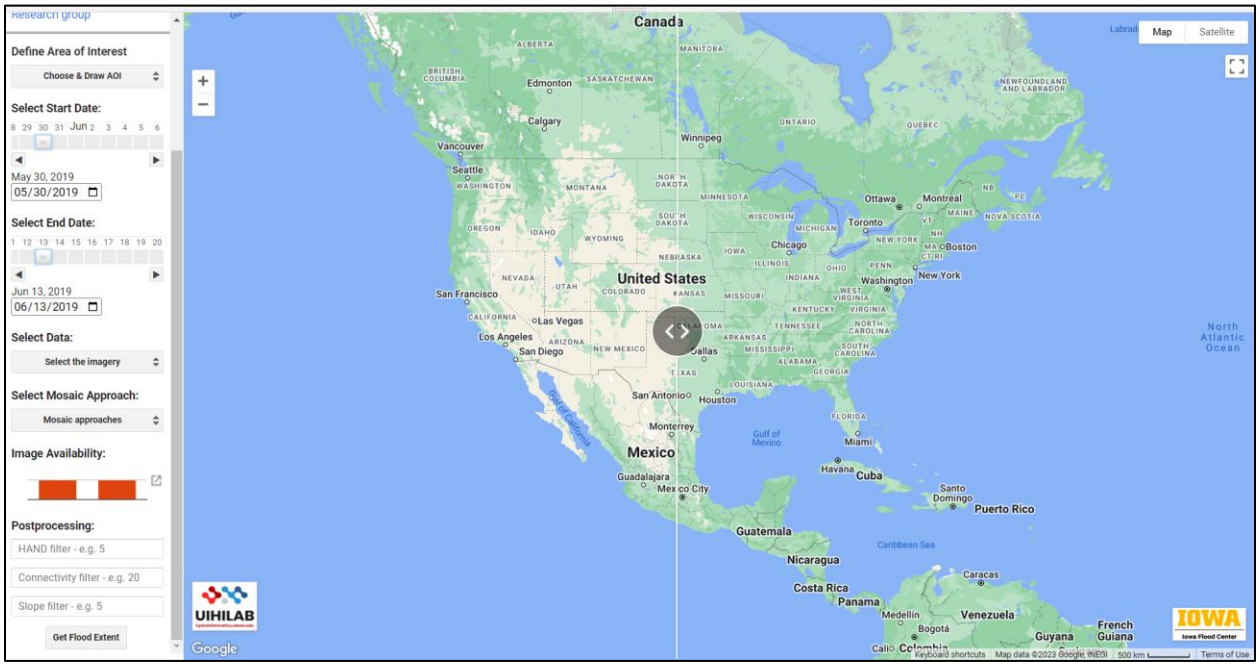

Figure 1. Application interface when it is loaded for the first time. From left to right is the left panel, left half of display (map) zone, and right half of the display (map) zone.

The right panel is for comparison and the map generated with widgets on this panel will be added on the right display zone to allow a comparison with the map on the left. The right panel has many similar items to those in the left panel, but items on different panels will function independently. Similar to the left panel, upon the creation of the first map from the right panel, there will be a QFR section added to the bottom of the right panel as well. Finally, we want to mention that there is a section for image download that is added to the bottom of the right panel upon the occurrence of the right panel, though it is not displayed in Figure 2 due to the screenshot display limitation. That is where maps generated from both left and right panels can be downloaded.

2.3. Data Preprocessing

As mentioned in the Introduction section, the SAR, L8, and S2 images provided on GEE are very close to a ready-to-analysis status thanks to the preprocesses done by GEE during the data integration. The preprocessing that will be done by the application is mainly the speckle noise removal for SAR, and cloud and cloud shadow removal for L8 and S2. The Refined Lee filtering approach with a 7×7 (7 pixel by 7 pixel) filter was adopted for denoising SAR images. The Refined Lee filter is a well-documented and efficient denoising algorithm for SAR images

(Brombacher et al., 2020; Chaudhary & Kumar, 2020; Kumar, 2021). The size of the moving window has also been proven robust in most cases by many previous studies (Chaudhary & Kumar, 2020; Wang et al., 2022).

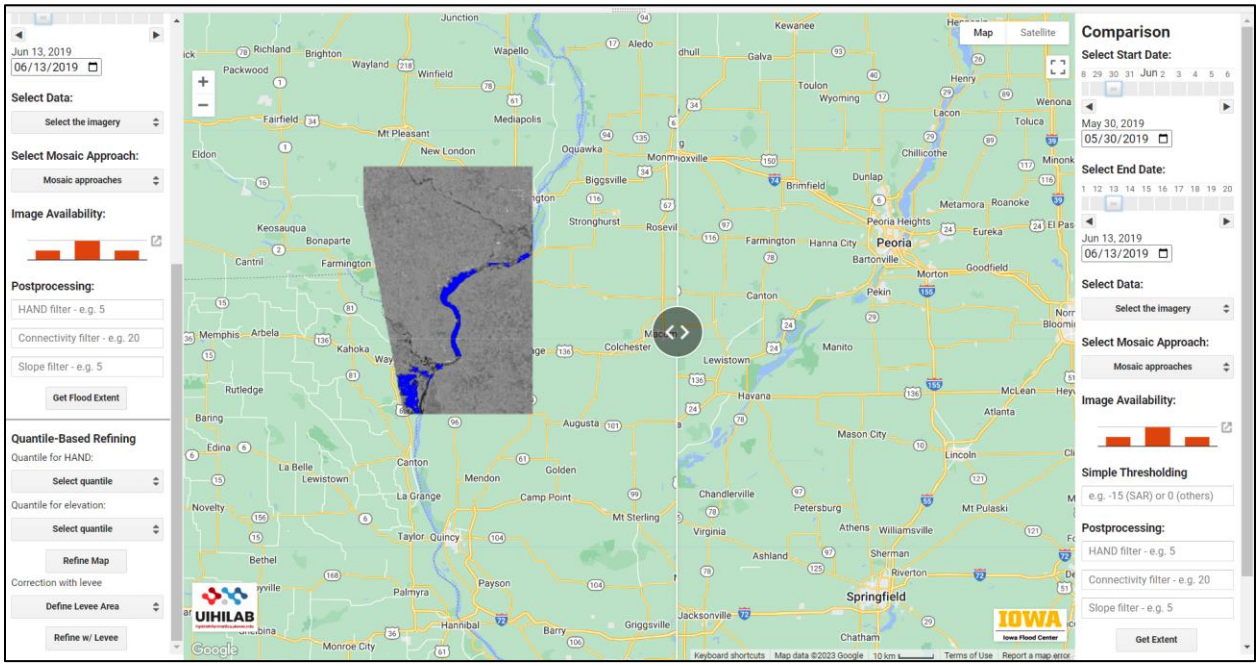

Figure 2. App interface after the creation of the first map. From left to right is the left panel, left half of display (map) zone, right half of the display (map) zone, and the right panel.

Cloud and cloud shadow removal is an active research topic over a few decades and there are numerous algorithms with different complexity proposed for this issue (Sankaraiah et al., 2023; Xiong et al., 2023; Zhai et al., 2018). Before applying any cloud or cloud shadow masks, MultiRS Flood Mapper filters S2 and L8 images and discard those that have more than 20% of the entire area being cloud. Then, it utilizes the QA60 plus the SCL band to detect the cloud and cloud shadow pixels in S2 images and utilizes the QA_PIXEL band for cloud and cloud shadow in L8 images. Band filtering is chosen among all available approaches because of its efficacy and no need for auxiliary data or heavy computation. Pixels identified as a cloud or cloud shadow will be masked and will not participate in any following processes. The Modified Normalized Difference Water Index (mNDWI) will then be calculated for those clear locations using the green and SWIR1 bands.

2.4. Water Extent Mapping and Adjustments

After preprocessing, thresholding will be applied to the VV band of SAR and to the mNDWI layer derived from L8 and S2 images to generate the rudimentary water extent map. The thresholding for the left panel (main panel) is dynamic Bmax Otsu. Bmax Otsu is an unsupervised thresholding method proposed by Markert et al., (2020) building on top of the improved Otsu thresholding method proposed by Cao et al., (2019) that is aimed at resolving the

possible failure of the bimodality assumption of the original Otsu method in large study areas. For any given study area, Bmax Otsu first applies a chessboard segmentation to divide the big area into small subregions; then it detects the bimodality (which can be interpreted as the distinguishability between water and non-water pixels) in each subregion and discard subregions from which no obvious bimodality is detected. Next, the Otsu threshold is determined for each subregion remaining from the previous step. Finally, an average of all thresholds obtained from the previous step will be used as the global threshold to tell apart water bodies from dry areas for the whole region (Cao et al., 2019).

The number of subregions of the chessboard division depends on the size of the area. Typically, the larger the area, the more subregions there should be. Considering that, we implemented the MultiRS Flood Mapper in a way that it can automatically adjust the size of each subregion of the division considering the size of the original study area. The thresholding for the right panel (comparison panel) is fixed thresholding, where a custom, fixed threshold is to be applied to the whole image. After the threshold step, standard post-processing will run automatically. It consists of three geomorphic conditions, when the pixels are too far vertically from a constant horizontal plane (such as river channels and lakes); not surrounded by enough adjacent pixels of the same kind; or when sitting on a steep hill, change the pixel category from a body of water to a dry area.

Normally, the Bmax Otsu plus a reasonable selection of postprocessing index will secure a satisfying water extent map in open water areas. While there could be some minor errors in areas with complex hydraulic and connectivity conditions, such as those near riverbank lines with complex shape or small ponds scattering on the land, there should not be major misclassifications. However, areas with dense vegetation can be different. As signals used by C-band SAR, S2, and L8 sensors are not able to penetrate vegetation crowns, images generated by those sensors cannot demonstrate surface conditions under vegetation canopies and may result in underestimations at locations blocked by the vegetation.

To solve this issue, MultiRS Flood Mapper integrates the QFR module proposed by Li and Demir, (2023a). QFR is a simple structured workflow that is originally aimed at resolving the underestimations due to the blocking of vegetation canopies. In short, QFR calculates a few candidate quantiles (e.g., 3/4 and 15/16) of HAND and elevation to represent geomorphic characteristics of water-body pixels on the original water extent map and uses those quantiles to change the category of some dry pixels if they are in locations where the HAND and elevation values are less than the computed quantiles. In other words, the category of dry pixels with similar geomorphic characteristics as water body pixels will be changed to water bodies.

In addition to being useful in densely vegetated areas, we further discover that the QFR can also help reconstruct water extent in regions blocked by cloud and cloud shadow for maps generated using L8 and S2. As discussed in the previous section, we omit RS image pixels that are covered by cloud and cloud shadow, and those locations will be masked on the original water extent map. Since geomorphology characteristics of those locations are stored on separate layers and will not be modified during the cloud filtering step, the QFR will be able to use those

characteristics to reconstruct the classification status for those contaminated locations, functioning act as a cloud removal algorithm. We will demonstrate how QFR helps resolve problematic classifications due to vegetation blocking as well as cloud contamination in section 3 with examples.

The QFR consists of three major steps: a) filling: this will change some dry (non-water bodies) or masked (cloud and cloud shadow contaminated) pixels on the original map to water bodies if they satisfy two quantile-based geomorphic conditions of DEM and HAND; b) refining: this is just another round of postprocessing using only HAND and connectivity to remove some of the newly introduced overestimations from the previous step; and c) optional correction: this will remove the hypercorrection from the filling step in situations where the water extent is under the control of hydraulic structures.

Figure 3 depicts the workflow of water extent extraction of both panels as well as the QFR postprocessing. It is worth mentioning that although the QFR module is shared by both panels, it functions independently on both sides. In other words, having the QFR called on one panel will not interfere with the module functioning on the other panel. The dash box around the QFR processing means that the module is optional, as the QFR is mainly for improving predictions in case of classification errors due to the blocking from dense vegetation and cloud and cloud shadow. For cases that are free from those negative impacts, QFR can be safely omitted. Another thing that is worth explaining is the arrow from the original water extent of both panels pointing to the *extent with filling* box. The way we drew it is just to indicate that the QFR starts from computing the quantiles when called by either side and does not mean there is information mixing between maps from the two different panels.

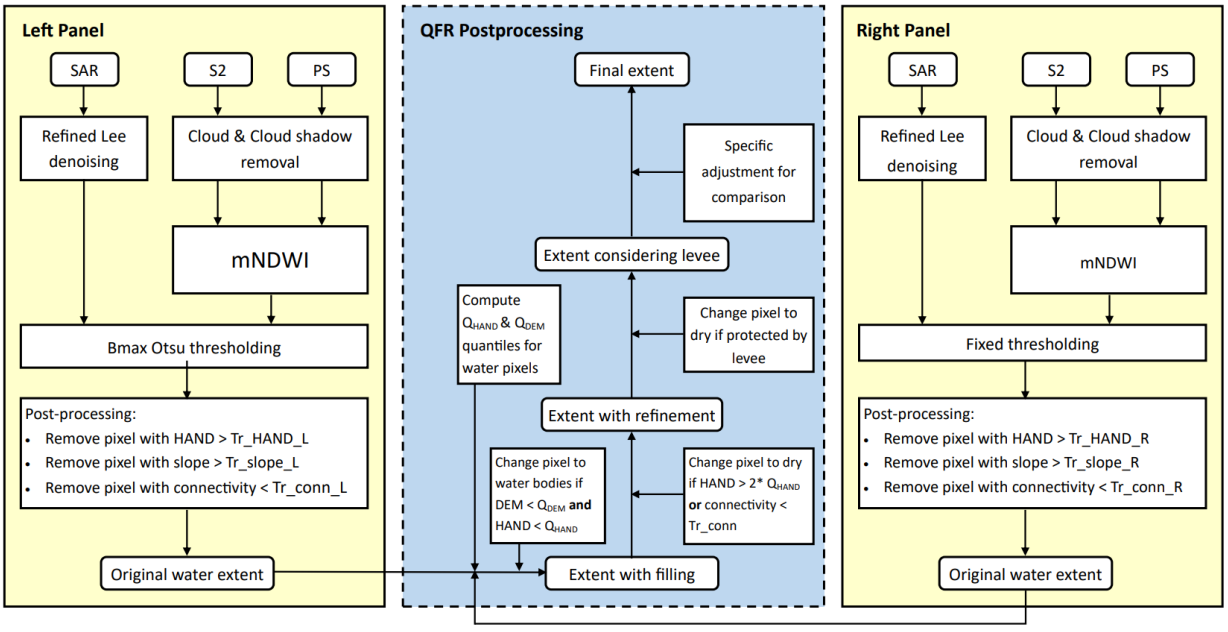

Figure 3. Workflow of water extent map generation with MultiRS Flood Mapper with both panels plus the QFR module

2.5. Two Panel Map Comparison

To facilitate comparison, most function modules were made sharable between the left and right panels. Meanwhile, they will work on both panels independently without interfering with each other. Specifically, selections for data, date range, mosaic approaches (creating a big image with multiple small ones found in the study region within a defined date range), postprocessing and QFR settings function independently on the left and right panels. Two exceptions are the area of interest and scope of regions controlled by hydraulic structures (levee scope, hereinafter). Modules called from the right panel will only work for the area of interest defined previously using the left panel. The study area of the right panel will be the same as the left panel. This is because the right panel is aimed at comparing water extent maps from those on the left that are generated with different configurations. The same applies to the levee scope. MultiRS Flood Mapper can simulate the influence of having hydraulic structures on both left and right maps, but the right panel will use the same scope defined previously with the left panel.

2.6. MultiRS Flood Mapper Usage

As mentioned in previous sections, the MultRS Flood Mapper runs on the cloud and is open to any potential users who have access to the Internet. No register or log-in is needed to use most functions provided by MultiRS Flood Mapper, except for one optional step at the very end of the entire workflow that may require users to have a valid Google Earth Engine account (explained at the end of step #3 of the left panel down below). Here, we will quickly go over the functional modules that are placed on the left and right panels. We encourage readers to check out the Quick Start Guide for the MultiRS Flood Mapper for a detailed walk-through of all modules on the interface and the corresponding functions and usages.

Major steps of the left and right panels are listed as below:

Initialize Water Extent Map (left panel):

Step 1. Data preparation: This step includes defining Area of Interest (AOI), selecting a date range, selecting image type (i.e., SAR in ascending, SAR in descending, L8, or S2), selecting mosaic approach to mix multiple images found inside the AOI during the selected date range by taking the minimum/maximum/average and so on, and defining the HAND, connectivity, and slope thresholds for the standard postprocessing.

Step 2. Generate a map and iterate as needed: With all items listed in Step 1 set, 'Get Flood Extent' function will generate a water extent map using parameters defined in Step 1. The resulting map will be added automatically to the left display zone as shown in Figure 1. All items in Step 1 are changeable and users may regenerate the map as needed.

Step 3. Apply the QFR postprocessing (optional): If users want to improve the map's accuracy for potential misclassifications due to the blocking of dense vegetation or cloud contamination, they can apply the QFR postprocessing. Users only need to select the quantiles for HAND and elevation, respectively. As mentioned previously, QFR changes the category for dry and masked pixels if those pixels are in areas where the HAND and elevation values are less than the HAND and elevation values of the existing water pixels that correspond to the two

quantiles. Therefore, the larger those quantiles, the more likely to have more dry and masked pixels changed to water pixels.

As pixels in low areas are more prone to changes during QFR compared to those in high lands, there could be hypercorrection in low areas where the original hydraulic conditions are under the control of artificial structures such as levees. To handle the constrained water extent and revise the hypercorrection, the area indicating the scope controlled by those structures will be used to revise the category of pixels inside the area (will be referred to levee scope hereafter). The MultiRS Flood Mapper supports a polygon with vertices defined manually by users and can also read the scope file if provided with a Google Earth Engine Asset ID for the file. Obviously, if the user wants to make their own levee scope file accessible to the MultiRS Flood Mapper through the Asset ID approach, they need to store the file under the Asset folder of their own Google Earth Engine account, whereas a manually drawn polygon, just like all other function modules in the MultiRS Flood Mapper, does not require the GEE account.

Step 4. Download maps (optional): The MultiRS Flood Mapper exports resulting maps in KML format. Users will find all resulting maps in the drop-down list in the Download Image subsection at the bottom of the right panel that pops out at the same time the first map from is generated at Step 2.

Generate Water Extent Map for Comparison (right panel):

The right panel only shows up upon the generation of the first map on the left panel, as it needs a target to compare its own results with. Generating maps for comparison is optional. The steps for generating maps on the right panel are almost identical with those on the left panel with two exceptions. One occurs at step #1, the right panel will utilize the AOI defined previously for the left panel, so we omitted the AOI defining module from the right panel. The other one is the levee scope. Similar to the AOI, the right panel will use the levee scope defined previously on the left panel.

3. Results and Discussion

In this section, we will demonstrate the usefulness of the MultiRS Flood Mapper by introducing its key functional modules with real-world examples. As mentioned in the previous section, the workflow in open water areas and densely vegetated or cloud contaminated areas can be different due to the blocking of vegetation canopies or clouds. We will show results in open water as well as blocked regions for a comprehensive demonstration of the application's capability.

3.1. Maps Generated with Different Mosaicking and Postprocessing Configurations

Figure 4 depicts water extent maps generated with S2 images captured in an AOI (in purple) near the border of Amapá and Pará states in Brazil with different mosaicking approaches applied to the same image collection obtained during the same time window. The area covers about 9,000 km^2 and contains two segments of the Amazon River. The four vertices of the AOI are [-51.55, -0.38] (top), [-50.91, -0.92] (right), [-51.51, -1.59] (bottom), and [-52.16, -1.03] (left), in decimal degrees of [longitude, latitude] under Web Mercator (EPSG: 3857) coordinate system.

The time range spans from May 30 to July 30, 2019. As shown in Figure 5, there are 16 S2 images that intersect the AOI. Figure 4 shows the water extent obtained with, from left to right, no mosaicking (take the first image), mosaicking by taking the maximum, by taking the average, and by taking the minimum. We noticed that from image (b) to (d), the S2 image visualization appears darker and darker. This is determined by the mathematical nature of the mosaicking approach we used (maximum, average, minimum, from (b) to (d)). Another thing we noticed in Figure 4 is that there are more white spots (cloud) on image (b) compared to (c) and (d). This is because cloud pixels are brighter and have larger pixel values than most of the other objects on the map. Therefore, clouds tend to accumulate when taking the maximum among images. Even though we applied cloud removal algorithms to those images, those algorithms often cannot guarantee removing all clouds from the scene and those cloud pixels will accumulate because of the maximum operation. Due to the cloud contamination, the water extent of the image (b) is very disconnected compared to (c) and (d).

Figure 4. Maps generated from the same image collection using different mosaicking approaches for the same AOI containing two Amazon River segments. a) no mosaicking (taking the first image); b) taking the maximum; c) taking the average; d) taking the minimum. The blue scope is the extracted water extent, the purple square is the scope of the AOI, the dark green is the visualization with red, green, and blue bands of the S2 image, and the white spots are clouds.

In addition, there are clear visual discrepancies between some locations versus the rest parts in some images, such as the little triangular region on the left-hand side of Figure 4 (b) and (c) and the upper part of Figure (d). Those are the spectral differences between different images in the 16-image collection from which we created the mosaic and is hard to avoid for feature-level fusions as we adopted in the MultiRS Flood Mapper. Decision-level fusion (extract water extent from each image and then mosaic the water extent map) can avoid the spectral discrepancy issue but comes with its own issue as well. For instance, the average between the water-body class and non-water-body class will be ambiguous. Additionally, it will result in a lot of misclassifications if taking the minimum and maximum in cases where there is little overlap between the water extent derived from different images. Finally, the decision-level fusion is far more computationally expensive than the feature-level fusion for large image collection, as it needs to go through each image to compute the water extent for mosaicking.

Mosaicking images that are captured temporally close to each other is a good practice to avoid the spectral discrepancy issue discussed above. Normally, RS images are generated as

satellites or other devices that carry sensors passing over in the air and scanning the Earth's surface. Images generated from the same scan with a few minutes in between during a short time duration tend to be more spectrally consistent due to similar illustration condition, viewing angle, and other factors that influence image's pixel values. In other cases, we do not recommend mosaicking images, as mosaicking images from different dates can be problematic due to noticeable spectral discrepancies. Additionally, we recommend defining an AOI that is well-targeted for the area to be studied, as the location of a single image can be quite random if the AOI is too large just as Figure 4 (a) shows.

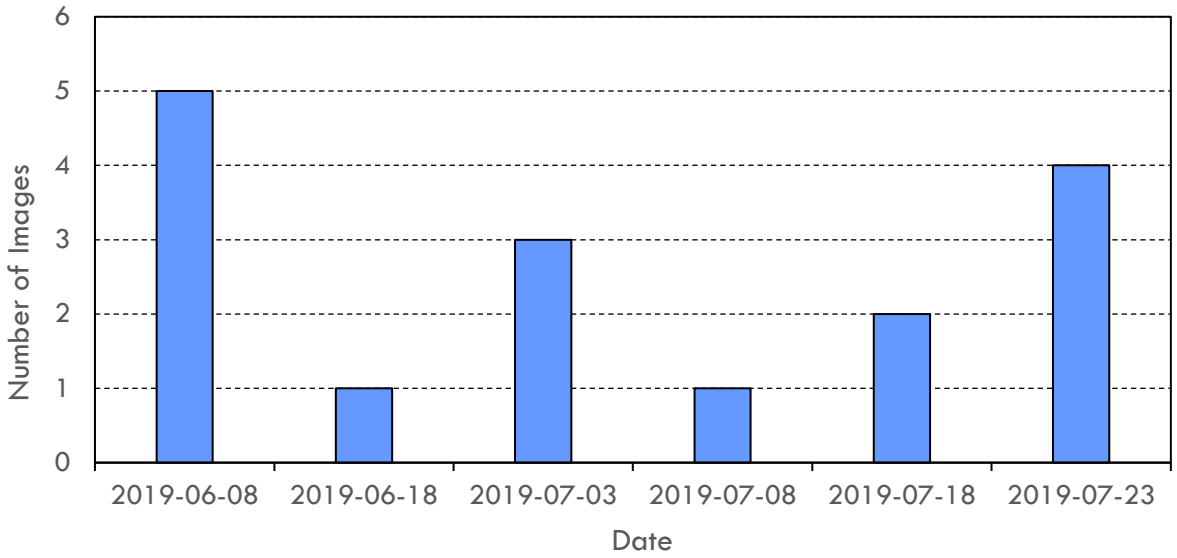

Figure 5. Image availability of S2 images within the study area in Figure 4 from May 30 to Jul 30, 2019

Figure 6 shows the water extent derived from the same S2 image (image (d) in Figure 4) with different postprocessing settings. As discussed in subsection 2.1, HAND describes how vertically close any hillslope pixels are to the permanent water bodies. Compared to Figure 6 (a), Figure 6 (b) applied a stricter HAND filter that eliminates any water bodies in areas where the HAND is larger than 1 (more than 1 m above the constant water bodies) and thus removed some pixels classified as water bodies on (a). Similarly, applying a stricter slope filter and ignoring any water bodies in areas with slope larger than 1 (image (d)) will also remove some pixels from the previous water-body class. For Image (c), we kept water bodies with a connectivity value larger than 80 (having more than 80 surrounding pixels that are also water bodies), and thus were also seeing some previous water pixels removed.

We noticed that changing filtering values for the postprocessing step would not result in much difference in the water extent. This is because the water extent will be mostly determined by the RS image as well as the approach used to extract water extent. This is favorable because, in general, we do not want significant changes during postprocessing steps. In other words, we want most pixels to be robust to changes in those postprocessing values so that we can eliminate

mismatches that are more sensitive while being able to keep most of the unaffected pixels that are highly likely to be good predictions. Though the sensitivity of results toward those values may vary from region to region, we believe, in general, postprocessing values selected from a reasonable range following the suggestions from existing literature will lead to satisfying results.

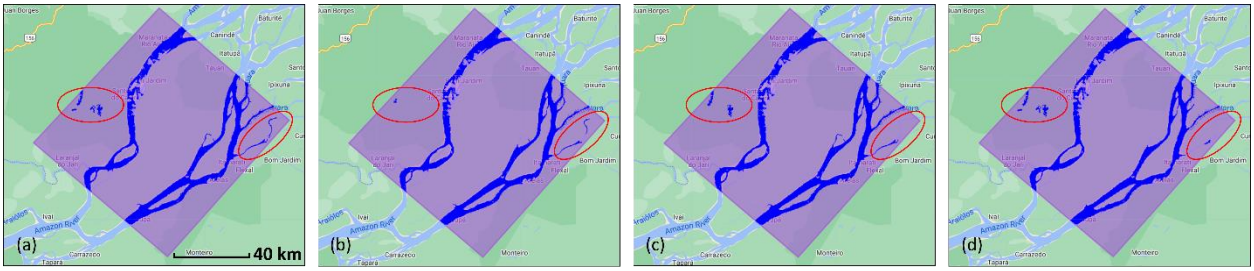

Figure 6. The water extent map derived from the same S2 image with different postprocessing settings. a) benckmark: HAND-5, connectivity-20, and slope-5; b) HAND-1, connectivity-20, and slope-5; c) HAND-5, connectivity-80, and slope-5; d) HAND-5, connectivity-20, and slope-1. Major differences occur in the area inside red circles.

3.2. Map Comparison between Panels

Figure 7 shows the water extent maps generated in a region on the border of Iowa and Illinois downstream to Quad Cities in the United States. The area covers about 600 km^2. The four vertices of the area are [-91.08, 41.20] (top-left), [-90.87, 41.20] (top-right), [-91.08, 40.88] (bottom-left), and [-90.87, 40.88] (bottom-right), in decimal degrees of [longitude, latitude] under Web Mercator (EPSG: 3857) coordinate system.

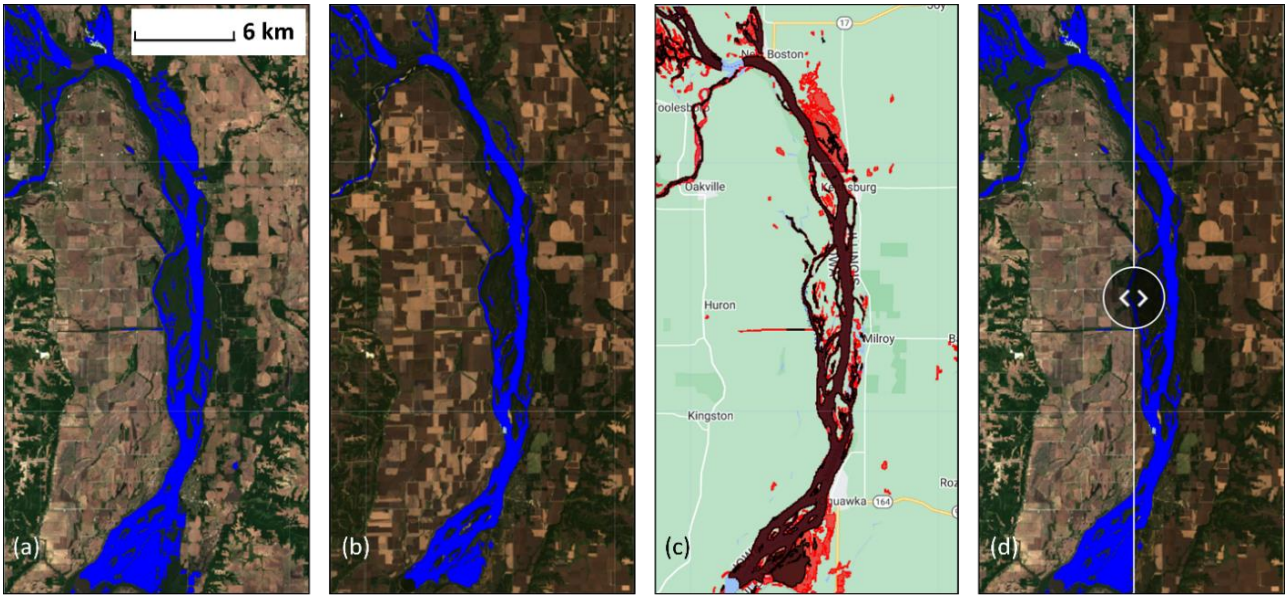

Figure 7. Water extent for the same region using images captured on different dates: a) water extent during a flooding event on 06/08/2019 on the left panel; b) water extent with no flood

warning on 10/07/2020 using on the right panel; c) overlapped extent from (a) in red and (b) in black; d) the visual comparison in the MultiRS Flood Mapper where scenes are stacked together

Figure 7 (a) shows the water extent generated with the left panel using an S2 image captured on June 8, 2019, during a flooding event. Figure 7(b) shows the water extent of the same area generated with the right panel using a L8 image captured on October 7, 2020, when no flooding was reported. We export the water extent (the blue scope) in KML files from (a) and (b) from the MultiRS Flood Mapper. Since KML files contain geospatial information, they will be placed in the correct location automatically if opened by software or applications with coordinate systems, such as QGIS, ArcGIS Pro and so on, just as what image (c) shows, with the water extent from (b) shown in black and that from (a) shown in red.

The visual comparison with the MultiRS Flood Mapper, as depicted by image (d), is quite easy as the left and right water extent is stacked together and sliding the division bar in the middle allows switching scenes to view with no effort. In addition to visual comparisons, KML files make it easy for quantitative comparisons as well. Those KML files indicate the actual scope of water extent on the Earth surface with the correct scale and therefore can easily be compared against shapefiles and geo-raster files.

3.3. Reducing Misclassifications Due to Cloud and Vegetation Blocking

We see from previous results and discussion that although cloud and cloud shadow removal algorithms were applied to optical images (i.e., L8 and S2) before the water extraction step, cloud cover can still be a problem sometimes as there is no guarantee that those algorithms, or in fact, any cloud removal algorithms, can be 100% successful. Things tend to get worse when mosaicking approaches that could lead to cloud accumulation were applied, as shown in Figure 4 (b).

As we discussed in subsection 2.3, QFR was originally introduced to improve classification in dense vegetation circumstances. It is a stronger postprocessing step (compared to the standard postprocessing steps discussed in subsection 3.1 for Figure 6) that corrects some of the misclassifications using statistical features of HAND and elevation at locations classified as water bodies on the problematic map. Figure 8 (a) is the same image as Figure 4 (b) where the connectivity of the resulting water extent is greatly influenced by the accumulated cloud on the scene, whereas Figure 8 (b) is the resulting map after applying the QFR to Figure 8 (a).

The quantiles selected for HAND and elevation are 15/16 and 3/4, respectively, meaning non-water pixels at locations with the HAND and the elevation values less than the HAND and elevation of the water bodies that correspond to those two quantiles will be recognized as water bodies. The selection of those quantiles may require some experience, but the general rule is that the more accurate the original map is, the less modification we will want to introduce, and therefore smaller quantiles should be used and vice versa. Our previous study based on analysis with dozens of SAR, PlanetScope, and Sentinel-2 image patches indicated that four quantiles, 3/4, 7/8, 15/16, and 31/32, are especially useful and can handle most cases (Li & Demir, 2023a).

We integrated those four quantiles for HAND and elevation in separate drop-down lists for users to choose from in MultiRS Flood Mapper.

Image 8 clearly shows the usefulness of QFR in improving the connectivity of water bodies and reducing noise. Another advantage of QFR, as we see, is that it does not introduce many new misclassifications when correcting the previous bad classifications. This will be the case for areas where the water connectivity is not constrained by artificial hydraulic structures, such as levees. In those cases, QFR can generate satisfying results without much need for extra steps to handle hypercorrections. However, in areas where the water extent is under control, hypercorrections may occur, just as what we will see in Figure 9.

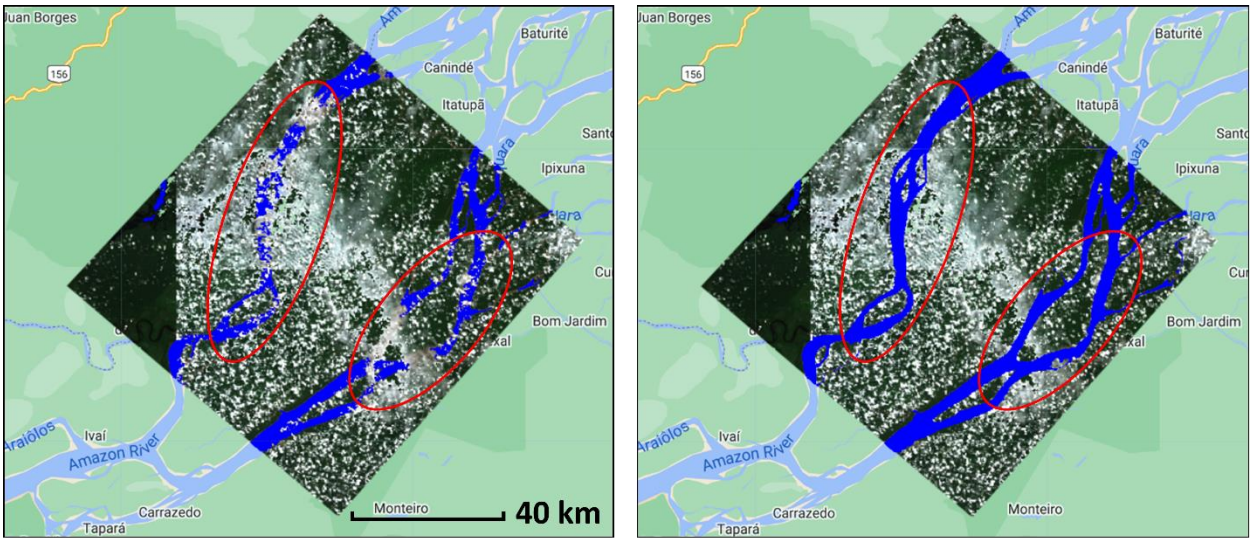

Figure 8. Water extent in areas with severe cloud contamination before (left) and after (right) applying the QFR postprocessing.

Figure 9 (a) is the same as Figure 7 (a). We export the extent map and stack it (in red) on top of the extent generated by HEC-RAS simulations (in black) in image (d). The HEC-RAS result comes directly from the work done by Gilles et al., (2012) and it depicts the inundation status at the time the S2 image was captured. As we see from image (d), there are underestimations in the RS-based map compared to the HEC-RAS simulation due to the blocking of dense vegetation on the scene (see also figures A1 (b) and (c) in the Appendix section for zoomed-in parts in the region). To solve this issue, we applied QFR. However, it turned out QFR introduced a lot of overestimations this time, as shown in image (b). Further investigation showed that the water extent in this area is in fact controlled by levees, as shown by Figure A1 (b) and (c) where there are clear line structures that are brighter and span along the river channels on both banks.

Usually, levees protect low areas from being inundated by water spreading out of river channels during riverine floods. Since those low areas are highly prone to change during the QFR, it therefore necessitates an extra step to consider the impact of those levees. Image (c) depicts the inundation built on top of what's shown in image (d) after considering the influence of levee. Image (e) shows when the water extent from (c) is placed on top of the HEC-RAS

extent. Comparing images (c) and (b), the extent after changing water bodies to dry within the scope controlled by the levee significantly constrained the spread of water bodies. Comparing the original water extent in (d) (in red), the revised extent in (e) (in red), and the HEC-RAS extent (in black in both (d) and (e)), it shows that the extent after applying QFR plus considering the levee-controlled area is overall more consistent with the HEC-RAS simulations and it gets rid of those many overestimations introduced during the QFR step shown in (b).

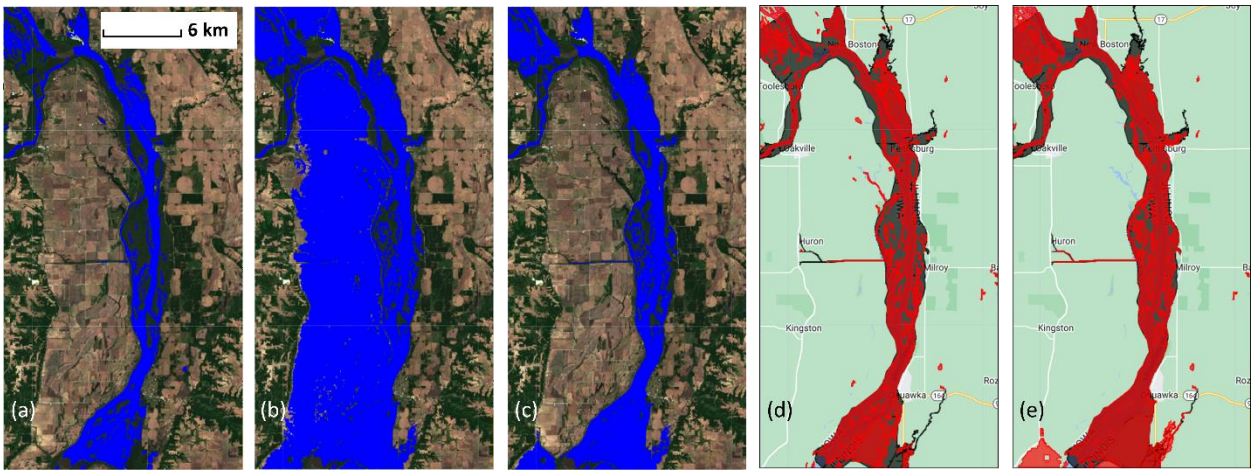

Figure 9. Water extent for the same regions using S2 image. a) The original extent; b) the extent after applying QFR; c) the extent after applying the levee to correct the hypercorrection from step (b); d) the extent of (a) in red stacked with HEC-RAS extent in black; e) the extent of extent of (c) in red stacked with the same HEC-RAS extent in black.

To sum up the QFR module, it can be used for improving the water extent map under the influence of both cloud and dense vegetation. One thing to keep in mind is that the whole configuration has to be consistent with the actual situation. Specifically, if water bodies are under controlled by some artificial structures, such as levees, we need to consider those influence to be able to get results that are consistent with the ground truth.

4. Conclusion

In this study, we proposed the MultiRS Flood Mapper, a cloud-based geospatial analysis application hosted on Google Earth Engine, with the motivation of creating an application that can handle the entire lifecycle of surface water extent mapping workflow and can serve a broader audience with different backgrounds and purposes. The MultiRS Flood Mapper incorporates the three most used RS imagery, namely, Sentinel-1 SAR, Landsat 8, and Sentinel-2, in the water mapping domain.

The custom AOI definition and mosaicking approach introduce additional flexibility and allow the application to serve various data processing and analytics needs. Results indicated that the mosaicking should be used with care due to the spectral discrepancies among images captured at different times and some mosaicking approach may result in cloud accumulation and

eventually leads to poor classifications. Typically, we suggested users conduct mosaicking among images captured within a narrow time slot where the outside conditions, such as illumination, and sensor configurations, such as viewing angle, are more consistent.

Results demonstrated the usefulness of the QFR module in improving classification accuracy under the influence of blocking from cloud and cloud shadow as well as dense vegetation. Results also showed the necessity of further adjustments to resolve hypercorrections introduced during QFR in regions with constrained hydraulic conditions. With the QFR module and the hypercorrection function, the MultiRS Flood Mapper can better adapt various geomorphic and geospatial characteristics and generate accurate maps for a broader group of target regions. The highly automated preprocessing modules, interactive standard postprocessing modules, and the two-panel-and-display-zone function allow easy and fast results evaluation and adjustments. In addition to the visual comparison between maps, the data exporting module makes it possible for quantitative comparison within and outside GEE.

While the MultiRS Flood Mapper takes a significant step towards the goal of creating cloud-based geospatial analysis tools that are powerful, flexible, and user-friendly, there is still room for improvement. For instance, it would be great to integrate RS images with higher resolution satellite datasets that are currently not available on GEE, such as PlanetScope. Another potential future step is to add more functional modules, such as drought mapping, to enrich the usability of the application.

5. Software Availability

Availability: The application is publicly available at
https://hydroinformatics.uiowa.edu/lab/floodmapper/
Developer: Zhouyayan Li, Ibrahim Demir
Software Tutorial: The tutorial of the MultiRS Flood Mapper is at
https://hydroinformatics.uiowa.edu/tutorials/floodmapper/

Acknowledgements

We would like to acknowledge the Iowa Flood Center for providing HEC-RAS flood maps in Figure 9 (d) and (e) for demonstration purposes.

References

Abdelmajeed, A. Y. A., Albert-Saiz, M., Rastogi, A., & Juszczak, R. (2023). Cloud-Based Remote Sensing for Wetland Monitoring—A Review. *Remote Sensing*, *15*(6), 1660. https://doi.org/10.3390/RS15061660/S1

Alabbad, Y., & Demir, I. (2022). Comprehensive flood vulnerability analysis in urban communities: Iowa case study. International journal of disaster risk reduction, 74, 102955.

Alabbad, Y., Yildirim, E., & Demir, I. (2023). A web-based analytical urban flood damage and loss estimation framework. Environmental Modelling & Software, 163, 105670.

Ali, A. U., & Ogie, R. (2017). Social media and disasters: Highlighting some wicked problems. *IEEE Technology and Society Magazine*, *36*(4). https://doi.org/10.1109/MTS.2017.2763450

Amani, M., Ghorbanian, A., Ahmadi, S. A., Kakooei, M., Moghimi, A., Mirmazloumi, S. M., Moghaddam, S. H. A., Mahdavi, S., Ghahremanloo, M., Parsian, S., Wu, Q., & Brisco, B. (2020). Google Earth Engine Cloud Computing Platform for Remote Sensing Big Data Applications: A Comprehensive Review. *IEEE Journal of Selected Topics in Applied Earth Observations and Remote Sensing*, *13*, 5326–5350. https://doi.org/10.1109/JSTARS.2020.3021052

Aravind, B., Atchyuth, S., Swain, R., & Das, P. (2023). *Near Real-time Flood Inundation and Hazard Mapping of Baitarani River Basin using Google Earth Engine and SAR Imagery*. https://doi.org/10.21203/RS.3.RS-3113777/V1

Bayar, S., Demir, I., & Engin, G. O. (2009). Modeling leaching behavior of solidified wastes using back-propagation neural networks. Ecotoxicology and environmental safety, 72(3), 843-850.

Berberian, L., Harris, K., Porter, M., & Waugh, E. (2023). *WET Water Resources: A Google Earth Engine Python API Tool to Automate Wetland Extent Mapping Using Radar Satellite Sensors for Wetland Management and Monitoring*.

Cikmaz, B. A., Yildirim, E., & Demir, I. (2023). Flood susceptibility mapping using fuzzy analytical hierarchy process for Cedar Rapids, Iowa. International Journal Of River Basin Management, 1-24. DOI: 10.1080/15715124.2023.2216936

Brombacher, J., Reiche, J., Dijksma, R., & Teuling, A. J. (2020). Near-daily discharge estimation in high latitudes from Sentinel-1 and 2: A case study for the Icelandic Þjórsá river. *Remote Sensing of Environment*, *241*, 111684. https://doi.org/10.1016/J.RSE.2020.111684

Buettig, S., Lins, M., & Goihl, S. (2022). WaterMaskAnalyzer (WMA)—A User-Friendly Tool to Analyze and Visualize Temporal Dynamics of Inland Water Body Extents. *Remote Sensing 2022, Vol. 14, Page 4485*, *14*(18), 4485. https://doi.org/10.3390/RS14184485

Cao, H., Zhang, H., Wang, C., & Zhang, B. (2019). Operational Flood Detection Using Sentinel-1 SAR Data over Large Areas. *Water 2019, Vol. 11, Page 786*, *11*(4), 786. https://doi.org/10.3390/W11040786

Chaudhary, V., & Kumar, S. (2020). Marine oil slicks detection using spaceborne and airborne SAR data. *Advances in Space Research*, *66*(4), 854–872. https://doi.org/10.1016/J.ASR.2020.05.003

Cheng, T., Ji, X., Yang, G., Zheng, H., Ma, J., Yao, X., Zhu, Y., & Cao, W. (2020). DESTIN: A new method for delineating the boundaries of crop fields by fusing spatial and temporal information from WorldView and Planet satellite imagery. *Computers and Electronics in Agriculture*, *178*, 105787. https://doi.org/10.1016/J.COMPAG.2020.105787

Chow, C., Twele, A., & Martinis, S. (2016). An assessment of the Height Above Nearest Drainage terrain descriptor for the thematic enhancement of automatic SAR-based flood monitoring services. *Https://Doi.Org/10.1117/12.2240766*, *9998*, 71–81. https://doi.org/10.1117/12.2240766

Cretaux, J. F., Calmant, S., Papa, F., Frappart, F., Paris, A., & Berge-Nguyen, M. (2023). Inland Surface Waters Quantity Monitored from Remote Sensing. *Surveys in Geophysics 2023*, 1–34. https://doi.org/10.1007/S10712-023-09803-X

Demiray, B. Z., Sit, M., & Demir, I. (2021). DEM super-resolution with efficientNetV2. arXiv preprint arXiv:2109.09661.

Estoque, R. C. (2020). A Review of the Sustainability Concept and the State of SDG Monitoring Using Remote Sensing. *Remote Sensing 2020, Vol. 12, Page 1770*, *12*(11), 1770. https://doi.org/10.3390/RS12111770

Gao, H., Donchyts, G., Winsemius, H., Schellekens, J., Erickson, T., Savenije, H., & Van De Giesen, N. (2016). Global 30m height above the nearest drainage. *Proceedings of the EGU General Assembly*. https://doi.org/10.13140/RG.2.1.3956.8880

Ghali, R., & Akhloufi, M. A. (2023). Deep Learning Approaches for Wildland Fires Using Satellite Remote Sensing Data: Detection, Mapping, and Prediction. *Fire 2023, Vol. 6, Page 192*, *6*(5), 192. https://doi.org/10.3390/FIRE6050192

Gilles, D., Young, N., Schroeder, H., Piotrowski, J., & Chang, Y. J. (2012). Inundation mapping initiatives of the iowa flood center: Statewide coverage and detailed urban flooding analysis. *Water (Switzerland)*, *4*(1), 85–106. https://doi.org/10.3390/w4010085

Godbout, L., Zheng, J. Y., Dey, S., Eyelade, D., Maidment, D., & Passalacqua, P. (2019). Error Assessment for Height Above the Nearest Drainage Inundation Mapping. *Journal of the American Water Resources Association*, *55*(4), 952–963. https://doi.org/10.1111/1752-1688.12783

Gorelick, N., Hancher, M., Dixon, M., Ilyushchenko, S., Thau, D., & Moore, R. (2017). Google Earth Engine: Planetary-scale geospatial analysis for everyone. *Remote Sensing of Environment*, *202*, 18–27. https://doi.org/10.1016/J.RSE.2017.06.031

Kabiraj, S., Jayanthi, M., Samynathan, M., & Thirumurthy, S. (2023). Automated delineation of salt-affected lands and their progress in coastal India using Google Earth Engine and machine learning techniques. *Environmental Monitoring and Assessment*, *195*(3), 1–15. https://doi.org/10.1007/S10661-023-11007-0/TABLES/4

Kim, B., Jung, J., Min, H., & Heo, J. (2021). Energy efficient and real-time remote sensing in AI-powered drone. *Mobile Information Systems*, *2021*. https://doi.org/10.1155/2021/6650053

Komolafe, A. A., Awe, B. S., Olorunfemi, I. E., & Oguntunde, P. G. (2020). Modelling flood-prone area and vulnerability using integration of multi-criteria analysis and HAND model in the Ogun River Basin, Nigeria. *Hydrological Sciences Journal*, *65*(10), 1766–1783. https://doi.org/10.1080/02626667.2020.1764960

Koo, Y., Xie, H., Mahmoud, H., Iqrah, J. M., & Ackley, S. F. (2023). Automated detection and tracking of medium-large icebergs from Sentinel-1 imagery using Google Earth Engine. *Remote Sensing of Environment*, *296*, 113731. https://doi.org/10.1016/J.RSE.2023.113731

Kumar, D. (2021). Urban objects detection from C-band synthetic aperture radar (SAR) satellite images through simulating filter properties. *Scientific Reports 2021 11:1*, *11*(1), 1–24. https://doi.org/10.1038/s41598-021-85121-9

Li, Z., & Demir, I. (2023a). Flood Sequence Mapping with Multimodal Remote Sensing Under the Influence of Dense Vegetation: Mississippi River Case Study. *EarthArXiv*. https://doi.org/10.31223/X5909M

Li, Z., & Demir, I. (2023b). U-net-based semantic classification for flood extent extraction using SAR imagery and GEE platform: A case study for 2019 central US flooding. *Science of The Total Environment*, *869*, 161757. https://doi.org/10.1016/J.SCITOTENV.2023.161757

Li, Z., Duque, F. Q., Grout, T., Bates, B., & Demir, I. (2023). Comparative analysis of performance and mechanisms of flood inundation map generation using Height Above Nearest Drainage. *Environmental Modelling & Software*, *159*, 105565. https://doi.org/10.1016/J.ENVSOFT.2022.105565

Li, Z., Mount, J., & Demir, I. (2022). Accounting for uncertainty in real-time flood inundation mapping using HAND model: Iowa case study. *Natural Hazards*, *112*(1), 977–1004. https://doi.org/10.1007/S11069-022-05215-Z

Li, Z., Xiang, Z., Demiray, B. Z., Sit, M., & Demir, I. (2023). MA-SARNet: A one-shot nowcasting framework for SAR image prediction with physical driving forces. ISPRS journal of photogrammetry and remote sensing, 205, 176-190.

Li, Z., & Demir, I. (2022). A comprehensive web-based system for flood inundation map generation and comparative analysis based on height above nearest drainage. Science of The Total Environment, 828, 154420.

Li, Z., & Demir, I. (2024). Better localized predictions with Out-of-Scope information and Explainable AI: One-Shot SAR backscatter nowcast framework with data from neighboring region. ISPRS Journal of Photogrammetry and Remote Sensing, 207, 92-103.

Liu, C. C., Shieh, M. C., Ke, M. S., & Wang, K. H. (2018). Flood Prevention and Emergency Response System Powered by Google Earth Engine. *Remote Sensing 2018, Vol. 10, Page 1283*, *10*(8), 1283. https://doi.org/10.3390/RS10081283

Markert, K. N., Markert, A. M., Mayer, T., Nauman, C., Haag, A., Poortinga, A., Bhandari, B., Thwal, N. S., Kunlamai, T., Chishtie, F., Kwant, M., Phongsapan, K., Clinton, N., Towashiraporn, P., & Saah, D. (2020). Comparing Sentinel-1 surface water mapping algorithms and radiometric terrain correction processing in southeast Asia utilizing Google Earth Engine. *Remote Sensing*, *12*(15), 2469. https://doi.org/10.3390/RS12152469

Moothedan, A. J., Dhote, P. R., Thakur, P. K., & Garg, V. (2020). Automatic Flood Mapping using Sentinel-1 GRD SAR Images and Google Earth Engine : A Case Study OF DARBHANGAH, BIHAR. *Recent Advances in Geospatial Technology & Applications, IIRS Dehradun, India*, *August*, 1–4. https://www.researchgate.net/publication/343539830

Muste, M., Lyn, D. A., Admiraal, D., Ettema, R., Nikora, V., & García, M. H. (2017). *Experimental Hydraulics: Methods, Instrumentation, Data Processing and Management: Volume I: Fundamentals and Methods*. CRC Press. https://www.google.com/books/edition/Experimental_Hydraulics_Methods_Instrume/YDgPEAAAQBAJ

Nobre, A. D., Cuartas, L. A., Hodnett, M., Rennó, C. D., Rodrigues, G., Silveira, A., Waterloo, M., & Saleska, S. (2011). Height Above the Nearest Drainage - a hydrologically relevant new terrain model. *Journal of Hydrology*, *404*(1–2), 13–29. https://doi.org/10.1016/j.jhydrol.2011.03.051

Pelich, R., Chini, M., Hostache, R., Matgen, P., Delgado, J. M., & Sabatino, G. (2017). Towards a global flood frequency map from SAR data. *International Geoscience and Remote Sensing Symposium (IGARSS)*, *2017-July*, 4024–4027. https://doi.org/10.1109/IGARSS.2017.8127883

Rennó, C. D., Nobre, A. D., Cuartas, L. A., Soares, J. V., Hodnett, M. G., Tomasella, J., & Waterloo, M. J. (2008). HAND, a new terrain descriptor using SRTM-DEM: Mapping terra-firme rainforest environments in Amazonia. *Remote Sensing of Environment*, *112*(9), 3469–3481. https://doi.org/10.1016/j.rse.2008.03.018

Sadiq, R., Akhtar, Z., Imran, M., & Ofli, F. (2022). Integrating remote sensing and social sensing for flood mapping. *Remote Sensing Applications: Society and Environment*, *25*, 100697. https://doi.org/10.1016/j.rsase.2022.100697

Sajan, B., Kanga, S., Singh, S. K., Mishra, V. N., & Durin, B. (2023). Spatial variations of LST and NDVI in Muzaffarpur district, Bihar using Google earth engine (GEE) during 1990-2020. *Journal of Agrometeorology*, *25*(2), 262–267. https://doi.org/10.54386/JAM.V25I2.2155

Sankaraiah, Y. R., Guru, M., Reddy, P., Venkata, O., Reddy, P., Muralikrishna, K., Chandra, K., & Sai, S. (2023). DEEP LEARNING MODEL FOR HAZE REMOVAL FROM REMOTE SENSING IMAGES. *Turkish Journal of Computer and Mathematics Education (TURCOMAT)*, *14*(2), 375–384. https://turcomat.org/index.php/turkbilmat/article/view/13662

Sit, M. A., Seo, B., & Demir, I. (2023). TempNet – temporal super-resolution of radar rainfall products with residual CNNs. *Journal of Hydroinformatics*, *25*(2), 552–566. https://doi.org/10.2166/HYDRO.2023.196

Sit, M., Demiray, B., & Demir, I. (2021). Short-term hourly streamflow prediction with graph convolutional gru networks. arXiv preprint arXiv:2107.07039.

Tamiminia, H., Salehi, B., Mahdianpari, M., Quackenbush, L., Adeli, S., & Brisco, B. (2020). Google Earth Engine for geo-big data applications: A meta-analysis and systematic review. *ISPRS Journal of Photogrammetry and Remote Sensing*, *164*, 152–170. https://doi.org/10.1016/J.ISPRSJPRS.2020.04.001

Torres Gil, L. K., Valdelamar Martínez, D., & Saba, M. (2023). The Widespread Use of Remote Sensing in Asbestos, Vegetation, Oil and Gas, and Geology Applications. *Atmosphere 2023, Vol. 14, Page 172*, *14*(1), 172. https://doi.org/10.3390/ATMOS14010172

Tripathy, P., & Malladi, T. (2022). Global Flood Mapper: a novel Google Earth Engine application for rapid flood mapping using Sentinel-1 SAR. *Natural Hazards*, *114*(2), 1341–1363. https://doi.org/10.1007/S11069-022-05428-2/FIGURES/14

Tsyganskaya, V., Martinis, S., Marzahn, P., & Ludwig, R. (2018). Detection of temporary flooded vegetation using Sentinel-1 time series data. *Remote Sensing*, *10*(8), 1286. https://doi.org/10.3390/rs10081286

Velastegui-Montoya, A., Montalván-Burbano, N., Carrión-Mero, P., Rivera-Torres, H., Sadeck, L., & Adami, M. (2023). Google Earth Engine: A Global Analysis and Future Trends. *Remote Sensing 2023, Vol. 15, Page 3675*, *15*(14), 3675. https://doi.org/10.3390/RS15143675

Waleed, M., Sajjad, M., Shazil, M. S., Tariq, M., & Alam, M. T. (2023). Machine learning-based spatial-temporal assessment and change transition analysis of wetlands: An application of Google Earth Engine in Sylhet, Bangladesh (1985–2022). *Ecological Informatics*, *75*, 102075. https://doi.org/10.1016/J.ECOINF.2023.102075

Wang, Y., Chen, W., Mao, X., & Lei, W. (2022). Terrain Classification of Polarimetric SAR Images Based on Optimal Polarization Features. *Proceedings - 2022 International Conference on Computer Engineering and Artificial Intelligence, ICCEAI 2022*, 400–403. https://doi.org/10.1109/ICCEAI55464.2022.00089

Xiang, Z., Demir, I., Mantilla, R., & Krajewski, W. F. (2021). A regional semi-distributed streamflow model using deep learning. EarthArxiv, 2152. https://doi.org/10.31223/X5GW3V

Xiong, Q., Li, G., Yao, X., & Zhang, X. (2023). SAR-to-Optical Image Translation and Cloud Removal Based on Conditional Generative Adversarial Networks: Literature Survey, Taxonomy, Evaluation Indicators, Limits and Future Directions. *Remote Sensing 2023, Vol. 15, Page 1137*, *15*(4), 1137. https://doi.org/10.3390/RS15041137

Yildirim, E., & Demir, I. (2022). Agricultural flood vulnerability assessment and risk quantification in Iowa. *Science of The Total Environment*, *826*, 154165. https://doi.org/10.1016/J.SCITOTENV.2022.154165

Yildirim, E., Just, C., & Demir, I. (2022). Flood risk assessment and quantification at the community and property level in the State of Iowa. International Journal of Disaster Risk Reduction, 77, 103106.

Zhai, H., Zhang, H., Zhang, L., & Li, P. (2018). Cloud/shadow detection based on spectral indices for multi/hyperspectral optical remote sensing imagery. *ISPRS Journal of Photogrammetry and Remote Sensing*, *144*, 235–253. https://doi.org/10.1016/J.ISPRSJPRS.2018.07.006

Zhao, J., Pelich, R., Hostache, R., Matgen, P., Wagner, W., & Chini, M. (2021). A large-scale 2005–2012 flood map record derived from ENVISAT-ASAR data: United Kingdom as a test case. *Remote Sensing of Environment*, *256*, 112338. https://doi.org/10.1016/J.RSE.2021.112338

Appendix

Figure A1 shows zoomed-in regions of Figure 9 (a) to demonstrate the dense vegetation in the study area. Note that it is easier to recognize the vegetation with the MultiRS Flood Mapper's interface, here we adjusted the brightness and contrast of (b) and (c) for easier visual recognition on the paper. Image (d) shows the scope of levee with orange polygon that we used to revise hypercorrections from QFR.

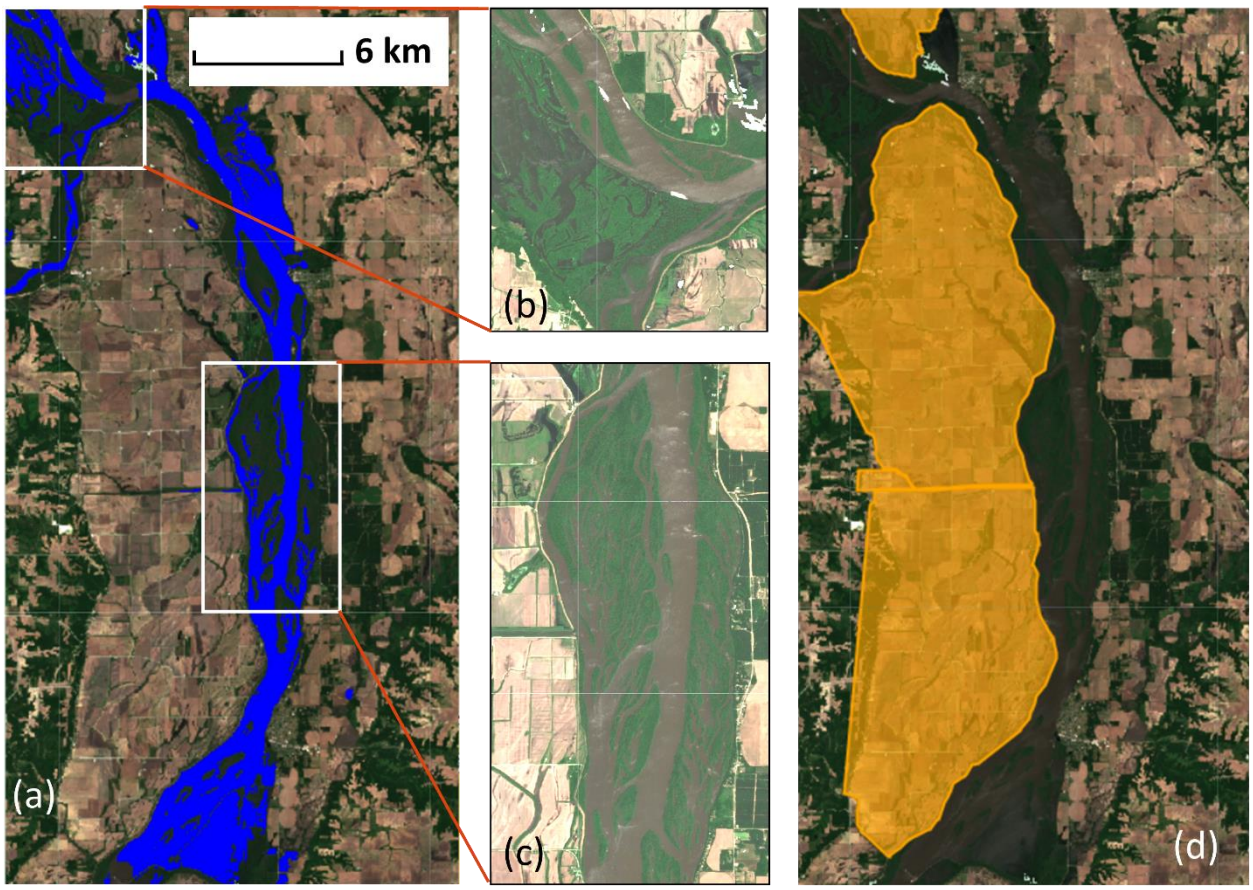

Figure A1. (a) Same image as Figure 9 (a); (b) & (c) zoomed-in of parts of image (a) in the white boxes; (d) the levee scope applied to revise hypercorrection from QFR